Available online at www.sciencedirect.com

ScienceDirect

Trans. Nonferrous Met. Soc. China 32(2022) 868−881

Transactions of Nonferrous Metals Society of China

www.tnmsc.cn

Corrosion and wear properties of TB2 titanium alloy borided by pack boriding with La_2O_3

De-yi QU, Dan LIU, Xin-yu WANG, Yong-hua DUAN, Ming-jun PENG

Faculty of Material Science and Engineering, Kunming University of Science and Technology, Kunming 650093, China

Received 18 February 2021; accepted 15 October 2021

Abstract: To improve the surface performance of TB2 alloy, pack boriding was performed at 1100 °C for 20 h with 4 wt.% La_2O_3. The composition and thickness of boride layer and corrosion and wear properties of borided TB2 alloy were measured. The results show that La_2O_3 can promote the growth, continuity, and compactness of boride layer, and the length of TiB whisker increases from 16.80 to 21.84 μm. The reason is that La_2O_3 can react with B to form La−B active groups and further to improve the growth of the boride layer. The wear and corrosion resistances of TB2 alloy are enhanced by boriding with La_2O_3. The wear mechanisms are adhesive wear and abrasive wear for unborided and borided TB2 alloys, respectively, and the corrosion mechanism is changed from local corrosion (unborided TB2 alloy) to uniform corrosion (borided TB2 alloy).

Key words: TB2 alloy; pack boriding; wear properties; corrosion performance

---

1 Introduction

Titanium alloys have been widely used in various industries due to their good corrosion resistance and high-temperature oxidation resistance, good biocompatibility, high specific strength and fatigue resistance [1,2]. However, the shortcomings of low hardness for titanium alloys limit their use in the field of wear resistance. One of the effective ways to improve the surface wear resistance and hardness of titanium alloys is to form boride layers on the surface by boriding [3]. Up to now, many efforts have been carried out on boriding methods, such as gas boriding, molten-salt boriding and laser pulse boriding [4−6]. Among these boriding methods, pack boriding is one of the most common methods for improving the surface properties of titanium alloy due to its simple process, low cost and dense boride layer [7].

Ti−5Mo−5V−8Cr−3Al titanium alloy (TB2 alloy) is a *β*-type titanium alloy with the chemical composition of 8 wt.% Cr, 5 wt.% V, 5 wt.% Mo, 3 wt.% Al and the balance Ti. TB2 alloy possesses the excellent cold workability, impact toughness, welding performance and plasticity, and tensile strength greater than 1400 MPa [8]. Therefore, TB2 alloy has great development potential and application prospects in structural components and fastening pieces of aerospace [9]. In order to overcome the shortcomings of TB2 alloy, i.e., low hardness and poor wear resistance, pack boriding is implemented on TB2 alloy. In our previous work, it has been found that the boride layer on TB2 alloy surface could increase the surface hardness up to 27.5 GPa, and decrease the coefficient of friction downward to 0.34 [10]. These improvements made the borided TB2 alloy possible to be used in fastening pieces and structural components of spacecraft and aircraft. Besides, the rare earth element oxide CeO_2 was added in the process of pack boriding, and the growth kinetic model of

---

Corresponding author: Yong-hua DUAN, Tel: +86-15987173606, E-mail: duanyh@kust.edu.cn;
Ming-jun PENG, Tel: +86-13888314332, E-mail: pmj5530594@kmust.edu.cn

DOI: 10.1016/S1003-6326(22)65839-4

boride layer was constructed [11]. The rare earth element can cause lattice distortion and increase the channel for boron diffusion [12]. Furthermore, the rare earth element can also increase the concentration of vacancy through the replacement mechanism, which promotes the diffusion of boron in the Ti phase [13]. In our previous work, the influence of type of rare earth oxide on boride layer of TB2 alloy was investigated, and the addition of La_2O_3 could obtain the relatively high surface hardness and low coefficient of friction of boride layer [14]; however, the reasons were not explained herein. In addition, more importantly, there are no other relevant literatures on borided TB2 alloy except our works. Therefore, the pack boriding with La_2O_3 is performed in this work, and the phase composition, morphology, hardness, wear and corrosion properties of the boride layer are further analyzed for the explanation of the wear and corrosion mechanisms. This can provide guidance for rare earth boriding of titanium and titanium alloys to improve the properties of surface boride layer.

2 Experimental

TB2 alloy (Northwest Institute for Nonferrous Metal Research, China) was cut into samples with 10 mm in diameter and 2 mm in thickness. The chemical composition of TB2 alloy is given in Table 1. Before the pack boriding, each sample was polished with 2000 mesh emery paper, and then cleaned by an ultrasonic cleaner in deionized water. Finally, the sample was covered with boride powder and sealed in an Al_2O_3 crucible. The boride powder was composed of 76 wt.% $Na_2B_4O_7$ (as transport medium, purity ≥98 wt.%, Tianjin Guangfu Fine Chemical Research Institute, China), 10 wt.% B_4C (as boron source, purity ≥99 wt.%, particle size ≤4 μm, Guangzhou Nano Chemical Technology Co., Ltd., China), 5 wt.% NaCl (as an activator, purity ≥99.5 wt.%, Guangdong Technology Research Center for Chemical Reagent, China), 5 wt.% Al (as reducing agent, purity ≥99.5 wt.%, particle size ≤5 μm, Changyuan County Mingyu Aluminum Co., Ltd., China), and 4 wt.% La_2O_3 (as a catalyst, purity ≥99.5 wt.%, particle size ≤5 μm, China Material Technology Co., Ltd., China).

In our previous work, the optimum parameters of pack boriding for TB2 alloy were 1100 °C, 20 h, and 4 wt.% La_2O_3 [14]. Therefore, a detailed investigation was conducted on TB2 alloy under these optimum parameters. Furthermore, the wear performance and corrosion performance of TB2 alloy after pack boriding were also discussed.

Table 1 Composition of TB2 alloy (wt.%)

Ti	Mo	V	Cr	Al	Fe	C	H	O	N
Bal.	5.10	4.96	8.22	2.91	0.30	0.05	0.015	0.015	0.04

The Bruker D8 Advance X-ray diffractometer (XRD) with Cu K_α monochromatic radiation was used to determine the phase composition of boride layer. The cross-section of the sample was polished with SiC sand paper and etched in 1 mL HF + 3 mL HNO_3 + 16 mL H_2O solution for observation of boride layer using Philips XL−370 scanning electron microscope (SEM). The wavelength-dispersive spectrometer (WDS) on JXA−823 electron probe microanalysis (EPMA) was employed to analyze B and Ti contents. The chemical valence of each element in boride layer was examined on a PHI5000 Versaprobe-II X-ray photoelectron spectroscopy (XPS) using a standard Al K_α X-ray source (300 W, 20 eV (pass energy)).

The SRV-IV micro-vibration friction and wear tester was used to test the wear performance of boride layer through reciprocating friction with load of 10 N, frequency of 20 Hz, reciprocating friction amplitude of 1 mm, and friction time of 1800 s. Meanwhile, Al_2O_3 ball with 6 mm in diameter was the abrasive material. The Agilent Nano Indenter G200 nanoindenter (the maximum load >500 mN, displacement resolution <0.01 nm, the maximum indentation depth >500 μm, and total displacement range of the indenter of 1.5 mm) was applied to measuring the hardness.

The corrosion performance of TB2 alloy and borided TB2 alloy in 3.5 wt.% NaCl and 5 wt.% H_2SO_4 solutions was performed at room temperature using CS310H electrochemical work-station, where platinum, sample, and saturated calomel electrode (SCE) work as the counter electrode, working electrode, and reference electrode, respectively. After the sample was immersed for 1 h, Tafel polarization curve, electrochemical impedance spectroscopy (EIS), and electrochemical noise (EN) vs open circuit potential (OCP) were tested. The scanning range and rate of Tafel polarization curve were from −1.5 to 0.5 eV and 0.1 mV/s, respectively. EIS was conducted with AC amplitude perturbation of 10 mV in a frequency range from 0.1 Hz to 0.1 MHz. Electrochemical potential and current noise were tested using an apparatus containing a noise module by placing samples in a shielding box. The input range and the maximum potential resolution of noise module are ±10 V and 10 mV, respectively.

3 Results and discussion

3.1 Characterizations of borided TB2 alloy

Figure 1 shows the X-ray diffraction (XRD) patterns of the borided TB2 alloy. For comparison, the XRD pattern of TB2 alloy without boriding is shown in Fig. 1(a). The XRD patterns of TB2 alloy borided at 1100 °C for 20 h without La_2O_3 and with La_2O_3 are plotted in Figs. 1(b) and 1(c), respectively. In Fig. 1(a), the as-received TB2 alloy is composed of α-Ti and β-Ti, and β-Ti is the main phase. As is known, α-Ti and β-Ti have the hexagonal closed-packed (HCP) lattice and the body-centered cubic (BCC) lattice, respectively, and there is a $\alpha \rightarrow \beta$ phase transformation at 882.5 °C [15]. Moreover, the densities of atomic arrangement in α-Ti and β-Ti are 0.74 and 0.68, respectively, indicating that the space volume of β-Ti (32%) is higher than that of α-Ti (26%). Thus, B atoms can diffuse into β-Ti more easily and rapidly, which can accelerate the growth of boride layers in β-Ti [16]. Besides, TiB whiskers grow ultra-fast in β-Ti due to three types of specific orientation relationships between β-Ti and TiB [17]. Therefore, the remaining α-Ti in TB2 alloy transforming to β-Ti after boriding at 1100 °C is beneficial to the growth of boride layer.

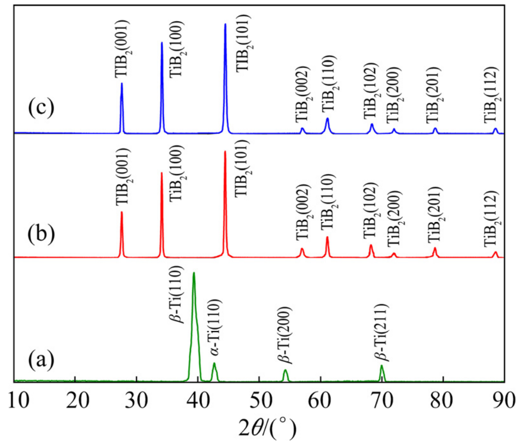

Fig. 1 XRD patterns of TB2 alloy under different boriding conditions: (a) TB2 alloy; (b) 1100 °C, 20 h; (c) 1100 °C, 20 h with 4 wt.% La_2O_3

From Figs. 1(b, c), the surface of borided sample consists of TiB_2 phase. According to our previous work, a thick boride layer that X-ray cannot penetrate is formed on the surface of the borided TB2 alloy, which causes the phases in the matrix not to be detected [11]. Here, the phases in Figs. 1(b, c) are the same, indicating that the boride layers obtained by boriding without and with La_2O_3 are thick, and the addition of La_2O_3 cannot change the phase composition of boride layer obviously. There are no XRD peaks of La_2O_3 in Fig. 1(c), which is due to the very small solubility of RE elements in titanium alloy. The alloying elements Mo, V, Cr, and Al are not detected in the boride layer. This may be due to the displacement of these elements by boron, as it is found in the case of boriding of Ti6Al4V alloy [7,18].

XPS test was performed on the samples borided with 4 wt.% La_2O_3 at 1100 °C for 20 h. Before the test, the sample was polished with 2000 mesh sandpaper to ensure cleanliness. Figure 2 shows the XPS scan spectrum with binding energy of 0−1400 eV. It is clear from Fig. 2 that, besides the XPS peaks of B and Ti, there are also XPS peaks of C and O elements. The peak of C 1s is located at 284 eV, which is the normal surface C contamination. The O peaks at the binding energies of 531.2 and 532.8 eV may originate from oxygen in the air, La_2O_3, and the decomposition product (B_2O_3) of $Na_2B_4O_7$. The alloying elements in TB2 alloy (Mo, V, Cr and Al) are also detected by XPS. However, these alloying elements can be displaced by boron and are not detected in the boride layer by XRD. Thus, these alloying elements may be trace in the boride layer.

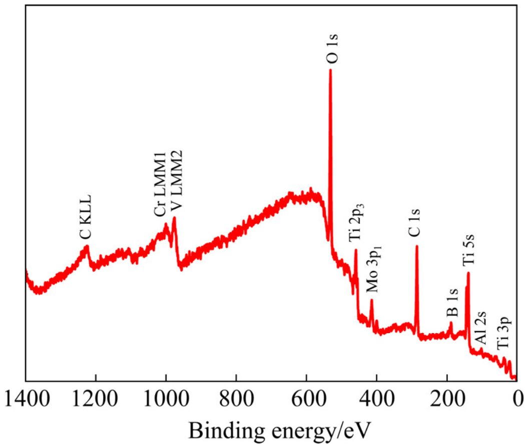

Fig. 2 XPS spectrum of borided samples

Figure 3 plots the XPS spectra of different elements in the boride layer of borided TB2 alloy. Herein, Figs. 3(a, b, c) show XPS peaks of Ti, B, and La elements, respectively. From Figs. 3(a, b), the Ti peak locates at 454.6 eV, and the B peak locates at 187.8 eV, which are consistent with the Ti $2p_{3/2}$ peak of 454.4 eV and the B 1s peak of 187.5 eV in the TiB_2 standard spectrum [19]. This indicates that there is TiB_2 in the boride layer, which is in good agreement with the result of XRD. The other two peaks of Ti are the peaks of TiO_2 [20]. The presence of TiO_2 in the boride layer comes from the reaction between TiB_2 and O_2 at room temperature [20]. Moreover, there are a B XPS peak at 192 eV (as shown in Fig. 3(b)) and an O peak at 532.8 eV (as shown in Fig. 2), which correspond to the binding energies of B_2O_3 [21]. The existence of B_2O_3 is due to the decomposition of $Na_2B_4O_7$. Due to the complex chemical environment of the pack boriding process, the detailed chemical reactions of active atomic boron [B] and Ti are as follows:

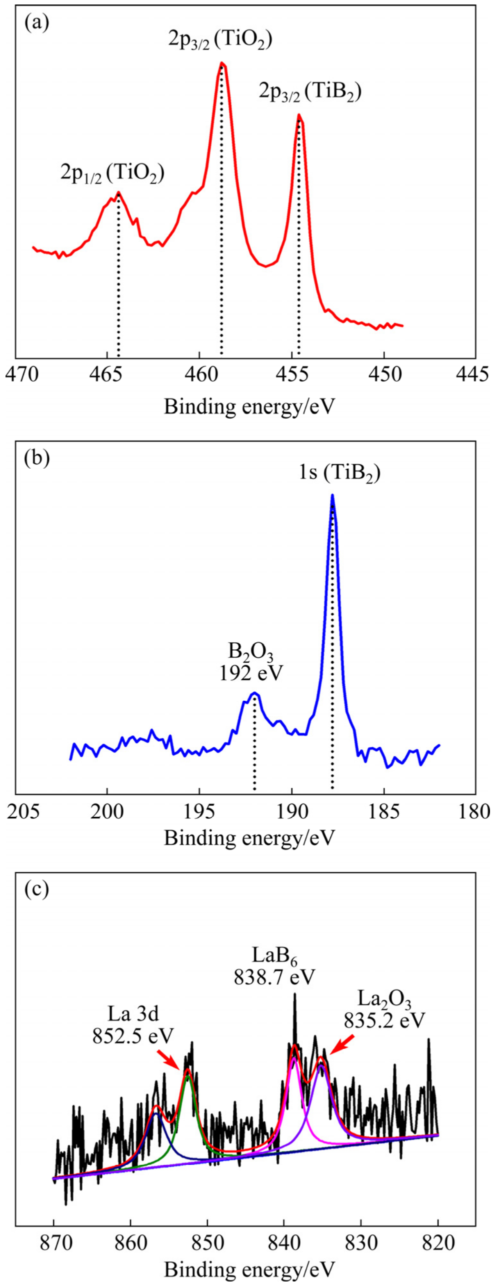

Fig. 3 XPS spectra of different elements: (a) Ti; (b) B; (c) La

$$Na_2B_4O_7 \rightarrow Na_2B_2O_4 + B_2O_3 \tag{1}$$

$$2Na_2B_2O_4 \rightarrow 4Na + 2B_2O_3 + O_2\uparrow \tag{2}$$

$$6Na + 2B_2O_3 \rightarrow 3Na_2O_2 + 4[B] \tag{3}$$

$$Ti + 2[B] \rightarrow TiB_2 \tag{4}$$

$$Ti + [B] \rightarrow TiB \tag{5}$$

$$TiB + [B] \rightarrow TiB_2 \tag{6}$$

After adding La_2O_3 in the boriding powder, besides the bove reactions (1)−(6), some new reactions occur. As is known, rare earth oxide CeO_2 reacts with [B] to form Ce−B and Ce−B−O compounds with high binding energy. In this work, we speculate that the rare earth element La_2O_3 reacts with [B] to form a compound of high binding energy in Fig. 3(c). Since the La content in the sample is small, the signal-to-noise ratio of the XPS spectrum of La 3d is low, so we used XPS peak software to perform peak separation and fitting of the spectrum. From Fig. 3(c), it can be seen that the core energy level orbit of La 3d is split obviously, which is a very special property of lanthanides. The binding energies corresponding to the four characteristic peaks of La are 856.7, 852.5, 838.7, and 835.2 eV, respectively. The La XPS peak at 856.7 eV is so weak that can be ignored. The La XPS peak at 852.5 eV corresponds to La 3p (853.0 eV). Here, the La XPS peak at 835.2 eV and that of O at 531.2 eV (as shown in Fig. 2) correspond to the XPS peaks of La_2O_3 [22], thereby confirming the existence of La_2O_3. The La XPS peak at 838.7 eV corresponds well with the reported XPS peak of La (836.8 eV) in LaB_6 [23]. Therefore, La_2O_3 reacts with [B] to form LaB_6. The corresponding chemical reactions after the addition of La_2O_3 are as follows [12]:

$$2La_2O_3 + 6Na \rightarrow 3Na_2O_2 + 4La \tag{7}$$

$$Ti + [B] \xrightarrow{La} TiB \tag{8}$$

$$TiB_2 + Ti \xrightarrow{La} 2TiB \tag{9}$$

$$La + 6[B] \rightarrow LaB_6 \tag{10}$$

Moreover, the reaction between La_2O_3 and B_2O_3 can produce LaB_6 by combustion synthesis [24]. However, the XRD pattern of the sample has no La_2O_3 and LaB_6 peaks, which proves that the La content in the boride layer is small.

The sample borided at 1100 °C for 20 h is selected to analyze the effect of La_2O_3 on boride layer. Figures 4(a, b) show the cross-sectional views of boride layer without La_2O_3 and with 4 wt.% La_2O_3, respectively. From Fig. 4, the boride layer without La_2O_3 is discontinuous and not compact, while that with 4 wt.% La_2O_3 is continuous and compact. We used the average of 10 points in Figs. 4(a, b) to measure the boride layer thickness and the whiskers length. After adding La_2O_3, the boride layer thickness is changed from 4.17 to 7.01 μm, and the whiskers length is increased from 16.80 to 21.84 μm. Thus, the addition of La_2O_3 can increase the boride layer thickness and the whiskers length, and can improve the continuity and compactness of boride layer, thereby effectively promoting the protective effect of boride layer on the matrix.

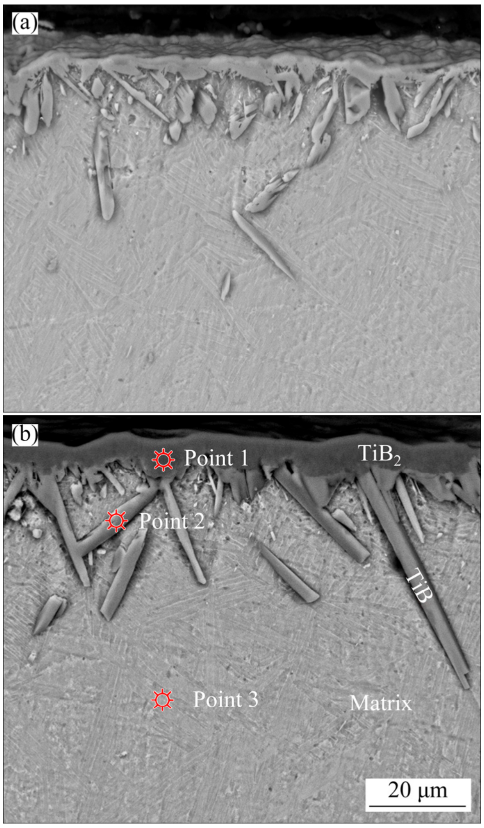

Fig. 4 Cross-sectional SEM morphologies of borided samples (1100 °C, 20 h): (a) Without La_2O_3 boriding treatment; (b) With 4 wt.% La_2O_3 (Points 1−3 represent the positions of WDS measurement)

As shown in Fig. 4(b), we selected a point at each of the boride layer, whisker and matrix to test the element content, and the results of the element contents are listed in Table 2. From Table 2, the atomic ratio of B to Ti at Point 1 is 1:1.95, which is very close to the atomic ratio of TiB_2. Combined with the phase composition obtained by XRD, the boride layer is composed of TiB_2. Similarly, the atomic ratio of B to Ti at Point 2 is 1:0.86, indicating that the whisker is composed of TiB. Moreover, Point 3 also contains a small amount of B, showing that B atoms can diffuse into the matrix.

Table 2 Element contents at different points in boride layer (at.%)

Point in Fig. 4	Ti	B
1	33.8496	66.1504
2	53.8778	46.1222
3	98.4268	1.5758

Figure 5 shows the distribution of B and Ti elements on the cross-section of the borided TB2 sample. From surface to matrix, the Ti content gradually increases, while the B content gradually decreases. Meanwhile, B element is only enriched at the boride layer and whiskers. Moreover, there is only a small amount of dispersion distribution of B inside the matrix. This is because of the boron source continuously decomposing active boron atoms or boron- containing active groups under the action of the reducing agent during the pack boriding process. These active boron atoms can react with Ti on the surface of the titanium alloy to form TiB_2. B atoms in TiB_2 layer continue to diffuse inward to form TiB with Ti; meanwhile, B atoms continue to diffuse into the matrix through interstitial diffusion. Thus, the additional B required for the growth of TiB is B atoms in TiB_2 layer, and the number of B atoms diffusing to Ti is mainly influenced by the contact area fraction of Ti and TiB_2 layer [25]. With the formation of a large amount of TiB whiskers beneath the TiB_2 layer, the contact area fraction of Ti and TiB_2 layer decreases, resulting in the decreased number of B atoms diffusing to Ti and the slow-down growth of TiB whiskers. The small amount of B element dispersed in the matrix may be caused by the formation of a large number of TiB whiskers that can hinder the diffusion of B atoms, resulting in the insufficient supply of B atoms.

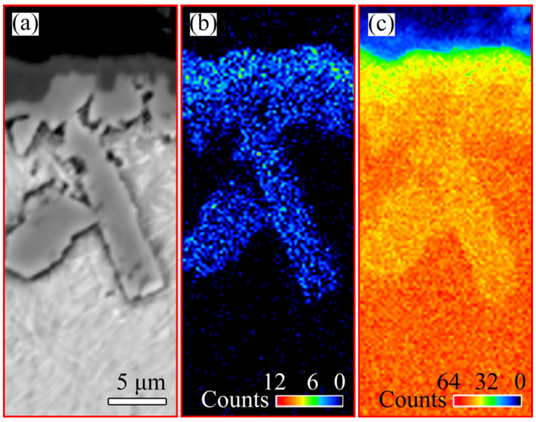

Fig. 5 Cross-sectional morphology (back scattered electron image) and element distributions of boronized layer: (a) Cross-sectional morphology; (b) B element; (c) Ti element

3.2 Analysis of Vickers microhardness and wear resistance

Table 3 lists the average hardness value of five corresponding points on TB2 alloy and borided samples. It is obvious that the average hardness of TB2 alloy without boriding treatment is 4.38 GPa, but the hardness of the matrix after boriding treatment reaches 5.0 and 4.97 GPa. The hardness of borided samples comparatively is higher than that of the TB2 alloy, which is attributed to the dispersion strengthening by B atoms and TiB particles dispersed in the matrix.

Table 3 Hardness values (GPa) of TB2 titanium alloy under different borided conditions

TB2	Borided sample (1100 °C, 20 h)			
	Without La_2O_3		With 4 wt.% La_2O_3	
	Boride layer	Matrix	Boride layer	Matrix
4.38	18.22	4.97	19.56	5.00

From Table 3, the hardness of boride layer is much higher than that of the matrix, which is due to the formation of TiB_2 and TiB phases with high hardness. Moreover, the main effect of La_2O_3 is the increase in continuity, compactness, and thickness of the boride layer, so the surface hardness of TB2 alloy with 4 wt.% La_2O_3 is the highest. The addition of La_2O_3 during the pack boriding process can promote the growth of the TiB_2 layer and TiB whiskers. TB2 alloy after boriding at 1100 °C for 20 h with 4 wt.% La_2O_3 has the continuous, compact, and thick TiB_2 layer and long TiB whiskers.

Since TB2 alloy is often used as spacecraft connectors and various rivets, screws and other fasteners due to its low density, high strength, and good corrosion resistance [26], the wear resistance of TB2 alloy is one of the important indicators to evaluate the comprehensive performance of the material surface. The wear performance of samples at room temperature and 250 °C are tested under dry friction and without lubricant. Figure 6 shows the wear morphologies of TB2 alloy and the alloy borided at 1100 °C for 20 h with 4 wt.% La_2O_3. Figure 6(a) represents the morphology of TB2 alloy after polishing, and Figs. 6(b, c) show the wear morphologies of TB2 at room temperature and 250 °C, respectively. Similarly, Fig. 6(d) shows the morphology of TB2 alloy after boriding, and Figs. 6(e, f) present the wear morphologies of TB2 alloy after boriding at room temperature and 250 °C, respectively.

From room-temperature wear morphologies of TB2 alloy in Fig. 6(b), it is obvious that the flakes appear on the surface of TB2 alloy, and there are a lot of deep grooves after wear test. Due to the relatively low surface hardness of TB2 alloy, Al_2O_3 ball can cut the surface of TB2 alloy, which causes matrix particles on the surface to fall off. Moreover, due to an increase in the contact temperature between Al_2O_3 ball and TB2 alloy during the reciprocation of Al_2O_3 ball, more TiO_2 particles are formed on the surface of TB2 alloy. The matrix particles adhering to Al_2O_3 ball and TiO_2 particles falling-off from the surface can destroy the sample surface in the friction process. Therefore, on the surface of TB2 alloy, there are many deep and long grooves caused by TiO_2 particles and some adhesions originated from matrix particles, which is a typical characteristic of abrasive and adhesive wears. During the entire wear process, the surface of samples is scratched under the combined action of abrasive wear and adhesive wear. According to the room-temperature wear morphology of TB2 alloy after boriding in Fig. 6(e), the surface of TB2 alloy after pack boriding is smoother than that of unborided TB2 alloy, and there are no obvious deep scratches. Because of the protection of boride layer, the borided TB2 alloy does not oxidize at room temperature, even at the increased contact temperature during the reciprocation of Al_2O_3 ball.

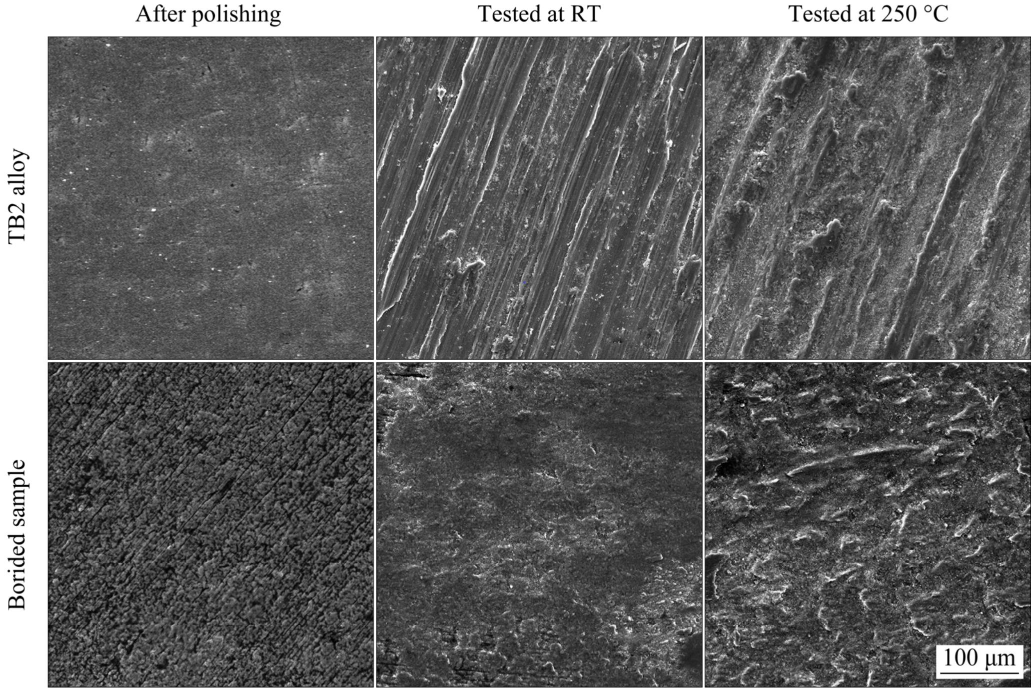

Fig. 6 Wear morphologies of TB2 alloy and borided sample (1100 °C, 20 h, with 4 wt.% La_2O_3) tested at different temperatures

However, the surface of the borided alloy is unsmooth, and thus, the boride micro-protrusions can be cut by Al_2O_3 ball to form abrasive particles. As a result, it can be seen in Fig. 6(e) that the abrasive wear plays a leading role in the friction and wear process of borided samples. Although adhesive wear is an important reason for the failure of the TB2 workpiece, pack boriding can effectively improve the wear resistance of TB2 alloy and extend the service life of spacecraft connectors and various rivets, screws and other fasteners.

In most cases, TB2 alloy is used in a relatively severe and high-temperature environment, so the wear experiments on TB2 alloy and borided samples at 250 °C are conducted. Figures 6(c, f) show the wear morphologies of TB2 alloy and the borided sample at 250 °C. It can be seen from Fig. 6(c) that the wide directional scratches appear on the surface of TB2 alloy at 250 °C, which is also due to the matrix particles and TiO_2 particles. The surface of the sample after pack boriding has no obvious directional scratches, but the surface becomes relatively uneven due to wear, as shown in Fig. 6(f). Since an Al_2O_3 ball is used as the counter surface, and both contacting surfaces (ball and borided surface) possess high hardness, an increase in the contact temperature during reciprocation is possible. At such high temperature, there are two possible chemical reactions in the high-temperature wear test, i.e., $2TiB_2 + 5O_2 \rightarrow 2TiO_2 + 2B_2O_3$ and $4TiB + 7O_2 \rightarrow 4TiO_2 + 2B_2O_3$ [27]. The boride particles cut by Al_2O_3 ball and TiO_2 particles are the abrasive particles to abrade on the surface of the borided TB2 alloy. However, the surface hardness of the borided TB2 alloy is high, and thus, no obvious scratches can be found.

Combined with the wear of samples under different conditions, for TB2 alloy, the adhesive wear plays a major role at room temperature, which causes large scratches on the sample surface. Moreover, after pack boriding at 1100 °C for 20 h with 4 wt.% La_2O_3, the abrasive wear plays a major role, which effectively improves the wear resistance of borided TB2 alloy. Besides, high temperature has a greater impact on the wear resistance of the sample, and the wear of the sample increases under high-temperature conditions.

Table 4 lists the mass changes of TB2 alloy and borided samples tested at different temperatures. From Table 4, the unborided TB2 alloy has a high wear mass and mass loss rate because of the low hardness. However, the borided layer with high hardness and good binding force is produced on the sample surface, and therefore, the mass loss rate reduces relatively. Under high-temperature conditions, both TB2 alloy and the borided sample have the poor wear resistance, significantly increased mass loss rate, and aggravated wear.

Table 4 Mass variations of TB2 alloy and borided sample during wear test at different temperatures

Sample	Test temperature	Mass before test/mg	Mass after test/mg	Mass loss/ mg	Mass loss rate/%
TB2	RT	4436.62	4435.01	1.52	0.00034
Borided		4295.53	4294.92	0.61	0.00014
TB2	250 °C	2088.31	2081.73	6.58	0.0031
Borided		2175.21	2170.80	4.41	0.0020

3.3 Electrochemical properties of boride layer

3.3.1 Potential polarization curve (Tafel curve)

Figure 7 shows the Tafel curves of TB2 alloy and TB2 alloy borided with 4 wt.% La_2O_3 at 1100 °C for 20 h in 3.5 wt.% NaCl and 5 wt.% H_2SO_4 solutions. Table 5 lists the electrochemical results of alloys in different solutions. From Fig. 7, at the beginning of cathode polarization, the current decreases as potential increases. From Fig. 7(a), in 3.5 wt.% NaCl solution, when the potential reaches −0.465 V, the cathode polarization ends and the anodic polarization begins. As the potential continues to rise to −0.453 V, the effect of the potential change on the current density becomes weak, and the alloy enters the passivation state. After the pack boriding, the trend of the polarization curve of TB2 alloy is consistent with that of the untreated TB2 alloy. The cathode polarization ends and the anode polarization begins when the potential reaches −0.243 V, and the alloy enters the passivation state when the potential is −0.226 V. Compared with the untreated TB2 alloy, the corrosion potential of the borided TB2 alloy in 3.5 wt.% NaCl solution is higher, and the polarization curve moves towards a positive direction. This means that the boriding treatment can hinder the corrosion of TB2 alloy and improve the corrosion resistance. Figure 7(b) shows the polarization curves of TB2 alloy and borided TB2 alloy in 5.0 wt.% H_2SO_4 solution. Compared with the unborided TB2 alloy, the Tafel curve moves towards the right, and the borided TB2 alloy has a larger φ_{corr} value (−0.460 V), indicating that the corrosion resistance of the borided TB2 alloy is improved in H_2SO_4 solution. Besides, the corrosion potentials of TB2 alloy and borided TB2 alloy in NaCl solution are more positive than in H_2SO_4 solution. Thus, the corrosion resistances of these alloys in NaCl solution are better than those in H_2SO_4 solution.

Although the electrochemical test of the borided TB2 alloy without La_2O_3 is not considered here, it can be inferred from the morphology of boride layer that TB2 alloy borided with 4 wt.% La_2O_3 has better corrosion resistance than TB2 alloy borided without La_2O_3. As is known, TiB has the significant role in the electrochemical behavior; that is, the monolithic TiB coating has better electrochemical behavior than TiB/TiB_2 coatings due to the fact that TiB can provide the stable passive film to protect the titanium matrix against the corrosion solution [28]. As shown in the morphology of boride layer (Fig. 4), the TiB whiskers in TB2 alloy borided with 4 wt.% La_2O_3 are longer and thicker than those in TB2 alloy

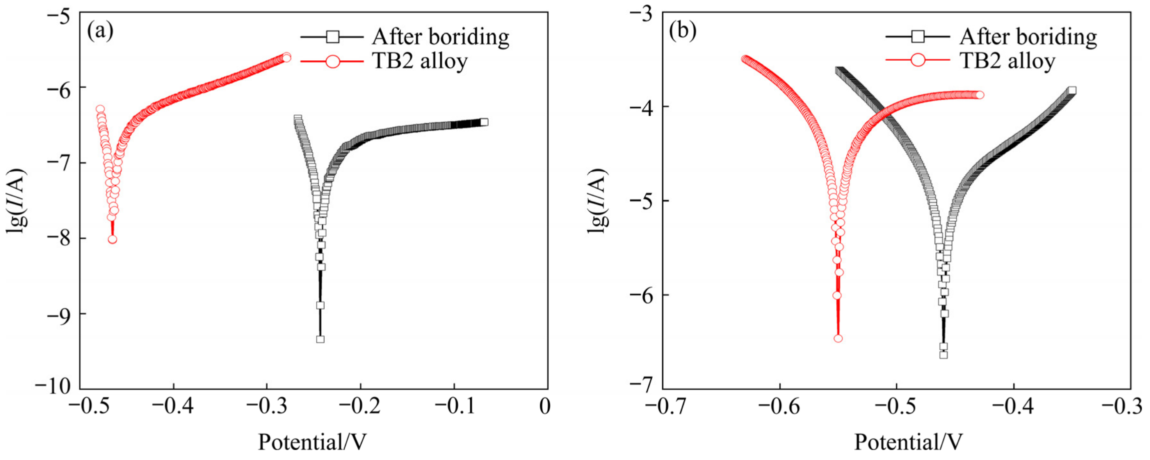

Fig. 7 Polarization curves of TB2 alloy in different solutions: (a) 3.5 wt.% NaCl solution; (b) 5.0 wt.% H_2SO_4 solution

Table 5 Electrochemical corrosion results of TB2 alloy and borided samples (with 4 wt.% La_2O_3 at 1100 °C for 20 h) in different solutions

Solution	Alloy	φ_{corr} (vs SCE)/V	J_{corr}/ (A·cm^{-2})
3.5 wt.% NaCl	TB2	−0.465	9.468×10^{-9}
	Borided	−0.243	4.603×10^{-10}
5.0 wt.% H_2SO_4	TB2	−0.550	1.880×10^{-4}
	Borided	−0.460	1.904×10^{-5}

borided without La_2O_3. This indicates that the TiB whiskers in TB2 alloy borided with 4 wt.% La_2O_3 can provide more stable passive film to protect the titanium matrix.

3.3.2 Electrochemical impedance spectroscopy

Figures 8 and 9 show the EIS results of TB2 alloy and borided TB2 alloy in 3.5 wt.% NaCl and 5.0 wt.% H_2SO_4 solutions, respectively. The Nyquist curves are shown in Figs. 8(a) and 9(a). A larger radius of Nyquist curve means a better electrochemical corrosion resistance [29]. From Figs. 8(a) and 9(a), the radius of the curve of borided sample is larger, indicating that the corrosion resistance of TB2 alloy is improved after boriding with 4 wt.% La_2O_3 at 1100 °C for 20 h. From Figs. 8(b) and 9(b), the larger |*Z*| value of impedance modulus represents the better corrosion resistance. Moreover, the magnitude of phase angle can indicate the ability of material to impede electrolyte penetration. The larger phase angle reflects the stronger impeding ability, indicating that the material has better corrosion resistance. TB2 alloys after boriding have the similar Nyquist curve and potential polarization curve. Therefore, the corrosion resistance of TB2 alloy can be enhanced by pack boriding effectively. Moreover, compared with H_2SO_4 solution, these alloys have larger radius of Nyquist curve and larger phase angle in NaCl solution, also indicating the better corrosion resistance of these alloys in NaCl solution.

3.3.3 Electrochemical noise

Figure 10 shows the electrochemical noise data of TB2 alloy and TB2 alloy borided with 4 wt.% La_2O_3 at 1100 °C for 20 h. There are relatively obvious transient peaks in Figs. 10(a, c), while there are none in Figs. 10(b, d). Generally, uniform corrosion makes current and potential

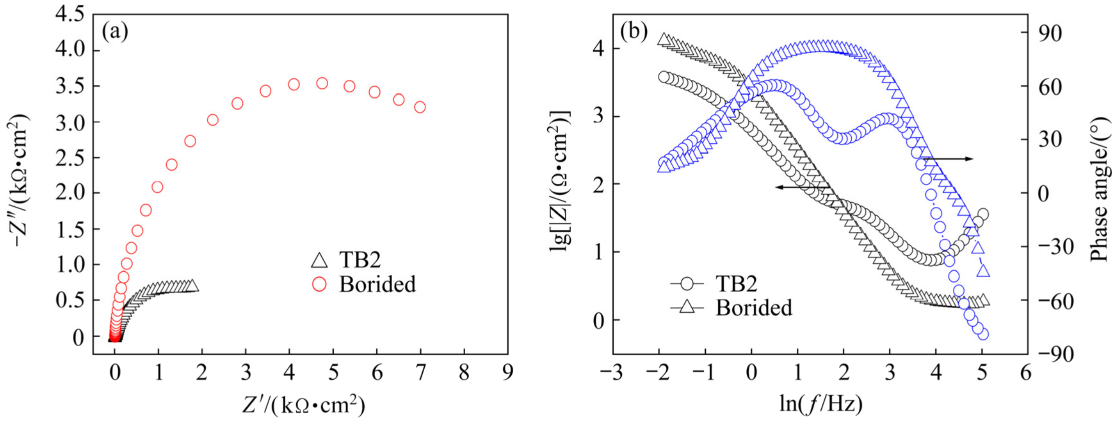

Fig. 8 EIS results of samples in 3.5 wt.% NaCl solution: (a) Nyquist plot; (b) Bode plot

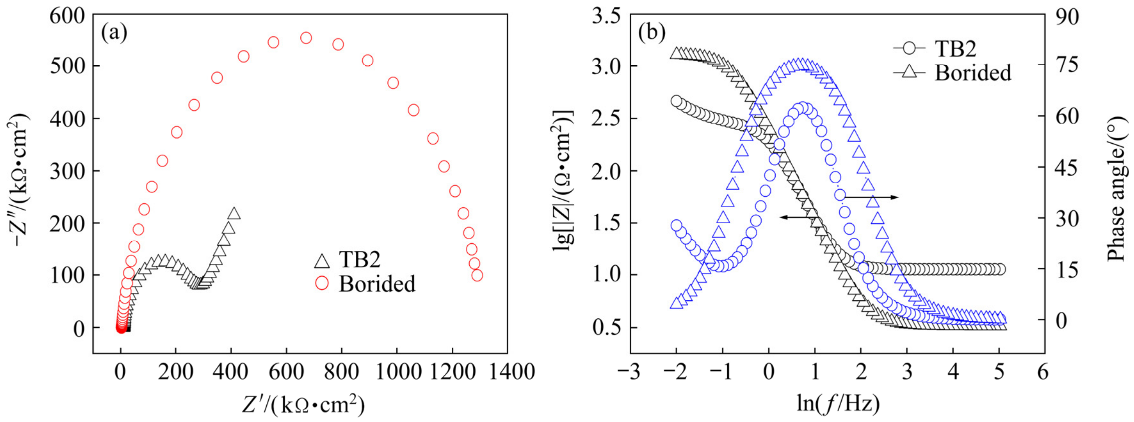

Fig. 9 EIS results of samples in 5.0 wt.% H_2SO_4 solution: (a) Nyquist plot; (b) Bode plot

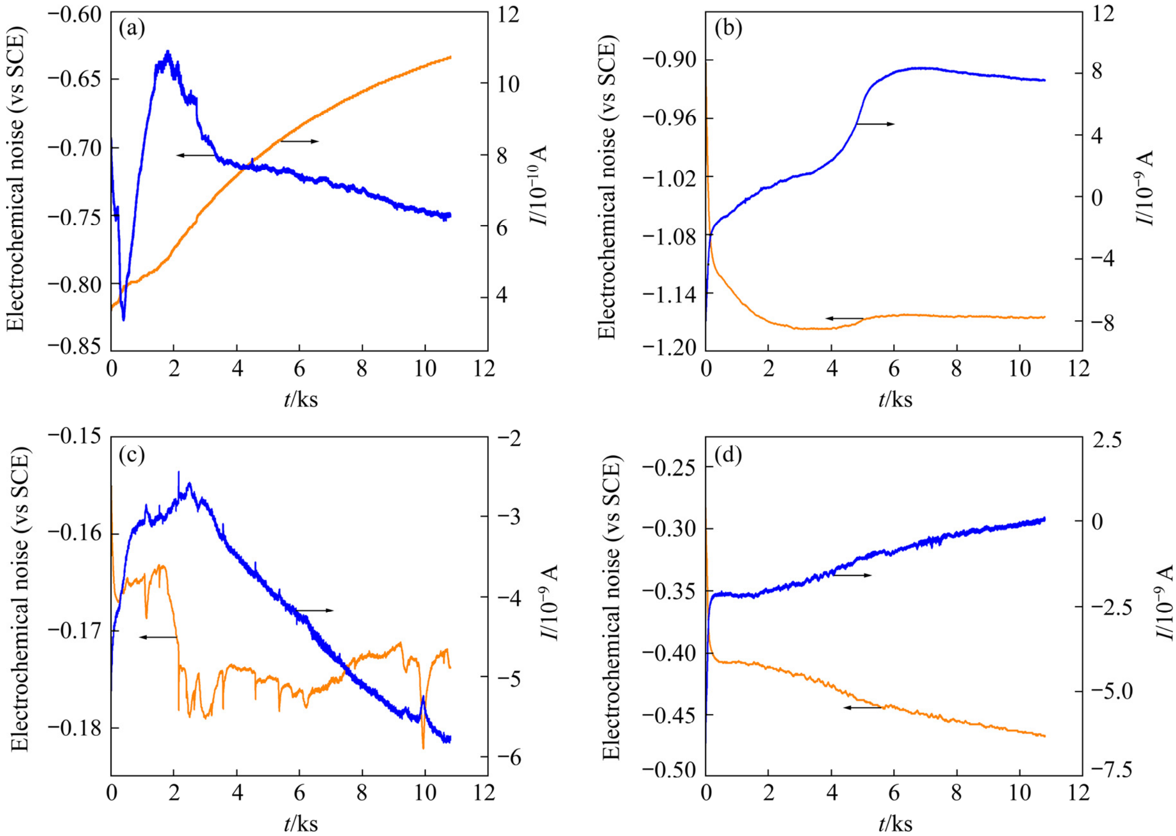

Fig. 10 Electrochemical noise data of sample in NaCl solution and H_2SO_4 solution: (a) TB2 alloy in NaCl solution; (b) Borided TB2 alloy in NaCl solution; (c) TB2 alloy in H_2SO_4 solution; (d) Borided TB2 alloy in H_2SO_4 solution

fluctuation frequency higher, and the curve has no obvious transient peak. The potential−time and current−time fluctuation curves caused by local corrosion have obvious transient-peak characteristics and randomness [30]. Thus, the unborided TB2 alloy has local corrosion in NaCl and H_2SO_4 solutions, while the borided TB2 alloy tends to be uniformly corroded.

3.3.4 Time-domain analysis

In the time-domain analysis, standard deviation S, noise resistance R_n, and pitting corrosion index P_I are often used to judge the corrosion type and corrosion rate [31]. R_n is the ratio of the standard deviation of potential noise S_V to current noise S_I, i.e., $R_n=S_V/S_I$, and the larger R_n reflects smaller corrosion rate and more difficult occurrence of corrosion [32]. Generally, $P_I=1.0$ indicates that pitting corrosion occurs; $1.0>P_I>0.1$ means that local corrosion occurs; $P_I=0$ shows that uniform corrosion occurs or the sample surface is in a passive state [31].

Table 6 lists the basic parameter values of the electrochemical noise of TB2 alloy under different conditions. In 3.5 wt.% NaCl and 5.0 wt.% H_2SO_4 solutions, the S_I value of current noise of the borided TB2 alloy is smaller than that of the unborided sample, while that of potential noise is converse. This indicates that the unborided TB2 alloy has a higher corrosion rate in these two solutions. Moreover, the P_I value of the unborided TB2 alloy is close to 0.6, and that of the borided TB2 alloy reaches about 0.2, indicating that the corrosion type of borided TB2 alloy is close to uniform corrosion, while the corrosion type of unborided TB2 alloy is local corrosion. This is consistent with the results of the polarization curve and the electrochemical impedance spectrum analysis. The corrosion resistance of TB2 alloy is improved by boriding from the time-domain analysis.

3.3.5 Frequency-domain analysis

The frequency-domain analysis can distinguish noise signals, which is its unique characteristic [33]. In this work, the law of current or potential changing with time (time-domain spectrum) is transformed into a power spectral density (PSD) curve using a fast Fourier transform (FFT) [34]. Then, the noise characteristics of the material are characterized by the height of the horizontal part of the PSD curve (white noise level, ψ_V and ψ_I), the frequency of the turning point of the curve (turning frequency), the slope of the inclined part of the curve (α), and the cutoff frequency of the curve (f_c). Figure 11 shows the PSD curves of TB2 alloy and borided TB2 alloy in different solutions. Theoretically, the PSD curve has a plateau at low frequencies and then has a linear relationship with f^{-n} as the frequency increases, and n is 2−4 normally [35]. Furthermore, the change rate of PSD in the high-frequency range can be used to distinguish the corrosion type. The higher change rate represents that the alloy surface may be in a state of passivation or uniform corrosion. Otherwise, it is in a state of pitting or local corrosion. From Fig. 11, all curves have a plateau in the low-frequency band, and show a linearly decreasing trend of repeated oscillations in the high-frequency band.

After fitting the data of PSD curves, the slope of the potential noise in high-frequency band (α) is obtained, and the results are listed in Table 7. The white noise levels ψ_V and ψ_I of potential noise and current noise are defined as the minimum values at the same frequency in the low-frequency range.

Table 6 Basic parameter values of time-domain analysis of electrochemical noise of TB2 alloy under different conditions

Basic parameter	3.5 wt.% NaCl solution		5.0 wt.% H_2SO_4 solution	
	TB2	Borided	TB2	Borided
S_V/V	0.0232	0.0554	0.00419	0.0223
S_I/A	3.37×10^{-9}	1.32×10^{-10}	9.87×10^{-10}	8.42×10^{-10}
R_n/(kΩ·cm^2)	0.00624	0.419	0.004242	0.0276
P_I	0.625	0.173	0.601	0.231

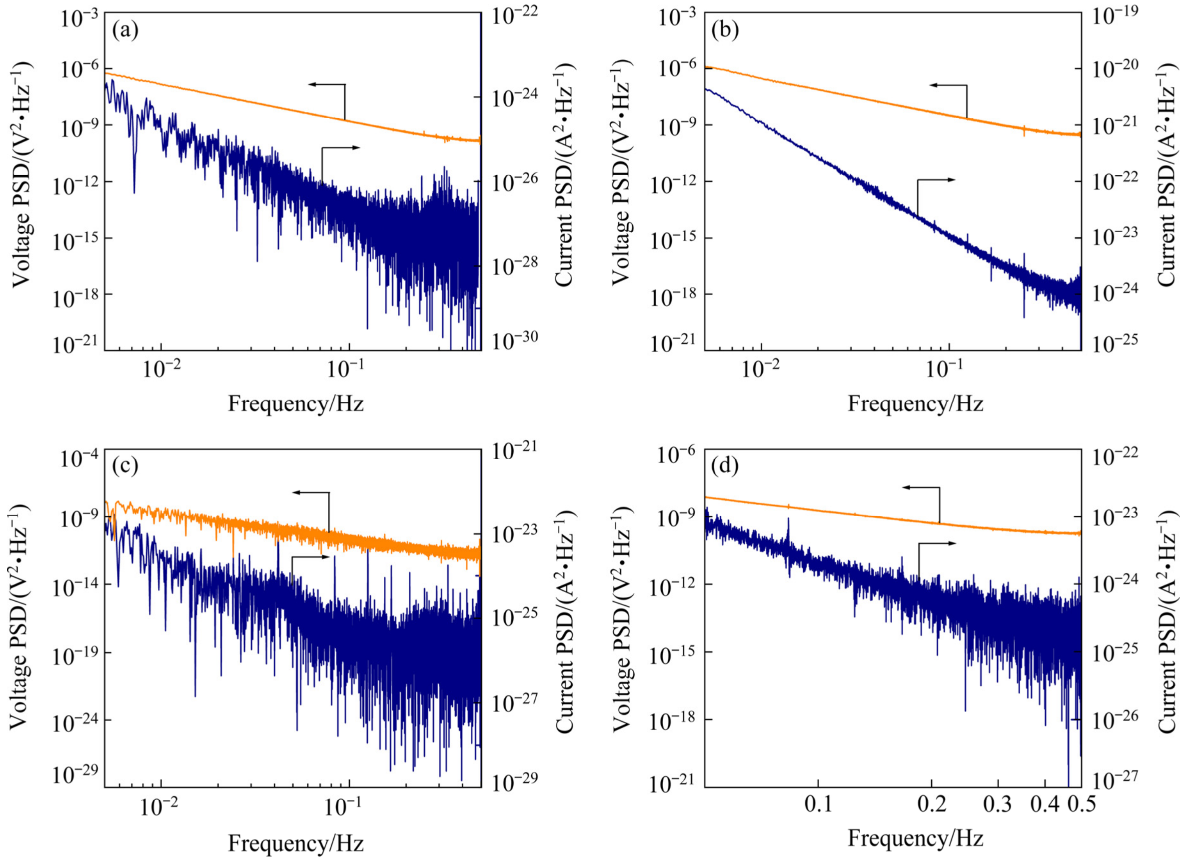

Fig. 11 PSD curves of TB2 alloy and borided TB2 alloy in different solutions: (a) TB2 alloy in NaCl solution; (b) Borided TB2 alloy in NaCl solution; (c) TB2 alloy in H_2SO_4 solution; (d) Borided TB2 alloy in H_2SO_4 solution

Here, we used the voltage and current PSD value ψ_V and ψ_I in the low-frequency range as an evaluation index for the corrosion resistance of the material, and the higher ψ_V and ψ_I correspond to the worse corrosion resistance of the material [36]. When the high-frequency slope α of potential noise is less than −40 dB/decade, uniform corrosion will occur on the surface. From Table 7, the potential white noises E_W of TB2 alloy in NaCl solution and H_2SO_4 solution are higher than that of the borided sample, thereby indicating that TB2 alloy has a better corrosion resistance after boriding. The high frequency slopes α of the PSD curve of the borided sample are −44.37 dB/decade and −44.31 dB/Hz in NaCl and H_2SO_4 solutions, respectively, which indicates that the corrosion type of the borided sample in NaCl and H_2SO_4 solutions is uniform corrosion. The α values of TB2 alloy in NaCl and H_2SO_4 solutions are higher than −40 dB/Hz, thereby indicating that the corrosion type of TB2 alloy is local corrosion. This also confirms that the borided TB2 alloy has better corrosion resistance than TB2 alloy. Moreover, the ψ_V and ψ_I values in NaCl solution are smaller than those in H_2SO_4 solution, while the α value in NaCl solution is larger than that in H_2SO_4 solution, which also indicates that these alloys possess the better corrosion resistance in NaCl solution than that in H_2SO_4 solution.

3.4 Corrosion morphology

Figure 12 shows the corrosion morphologies of TB2 alloy and borided TB2 alloy in 3.5 wt.% NaCl and 5.0 wt.% H_2SO_4 solutions. It is easy to see from Fig. 12 that the TB2 alloy has undergone serious corrosion in these solutions, and many obvious etch pits appear on the surface, especially in H_2SO_4 solution; while the etch pits on the surface of the borided TB2 alloy decrease significantly. According to the results of XRD and SEM analysis, a dense and hard boride layer is formed on the

Table 7 Frequency domain analysis results of TB2 alloy and borided TB2 alloy in different solutions

Basic parameter	3.5 wt.% NaCl solution		5.0 wt.% H_2SO_4 solution	
	TB2	Borided	TB2	Borided
$\Psi_V/(V^2\cdot Hz^{-1})$	4.63×10^{-6}	1.47×10^{-7}	5.65×10^{-6}	8.08×10^{-7}
$\Psi_I/(A^2\cdot Hz^{-1})$	3.55×10^{-21}	4.49×10^{-21}	8.69×10^{-21}	8.13×10^{-21}
$\alpha/(dB\cdot Hz^{-1})$	−35.46	−44.37	−25.13	−44.31

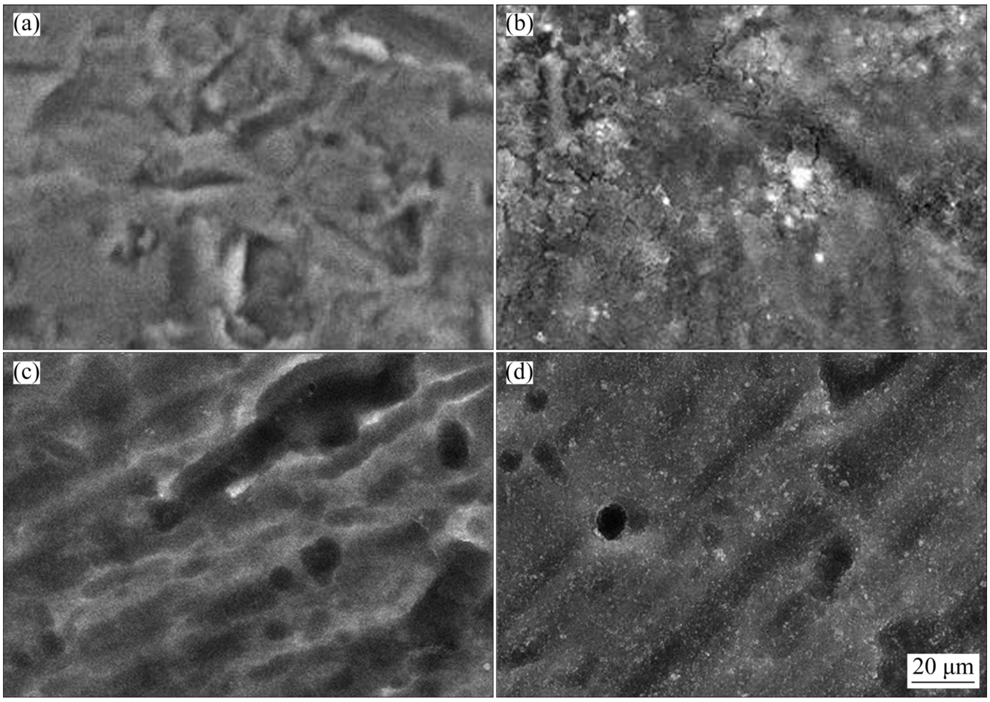

Fig. 12 Surface morphologies of sample after corrosion in 3.5 wt.% NaCl (a, b) and 5.0 wt.% H_2SO_4 solutions (c, d): (a, c) TB2 alloy; (b, d) Borided TB2 alloy

surface of TB2 alloy after boriding, which can effectively protect the matrix. During the corrosion process, the boride layer first contacts and reacts with the corrosive medium, which can effectively make the corrosion rate slow down. Moreover, the dense boride layer can hinder the passage of the corrosive medium to prevent the matrix from contacting the corrosive medium, which effectively improves the corrosion resistance of TB2 alloy. Therefore, the borided TB2 alloy has better corrosion resistance, which is consistent with the results of the Tafel curve, EIS, and EN analysis.

4 Conclusions

(1) After pack boriding at 1100 °C for 20 h with 4 wt.% La_2O_3, a dense boride layer composed of TiB_2 layer and TiB whiskers is formed on the TB2 alloy surface, and TiB whisker length increases to 21.84 μm.

(2) The surface hardness of borided TB2 alloy can be greatly improved to 19.56 GPa by the addition of La_2O_3.

(3) The wear mechanisms are adhesive wear and abrasive wear for unborided and borided TB2 alloys, respectively.

(4) The corrosion mechanism is changed from local corrosion (unborided TB2 alloy) to uniform corrosion (borided TB2 alloy).

Acknowledgments

The authors are grateful for the financial support from the National Natural Science Foundation of China (No. 51761023).

References

[1] HAGHIGHI S E, LU H B, JIAN G Y, CAO G H, HABIBI D, ZHANG L C. Effect of α'' martensite on the microstructure and mechanical properties of beta-type Ti−Fe−Ta alloys [J]. Materials and Design, 2015, 76: 47−54.

[2] BOYER R R. An overview on the use of titanium in the aerospace industry [J]. Materials Science and Engineering A, 1996, 213: 103−114.

[3] PENG Ming-jun, DUAN Yong-hua, MA Li-shi, SHU Bai-po. Characteristics of surface layers on Ti6Al4V alloy borided with CeO_2 near the transition temperature [J]. Journal of Alloys and Compounds, 2018, 769: 1−9.

[4] MAKUCH N. Influence of nickel silicides presence on hardness, elastic modulus and fracture toughness of gas-borided layer produced on Nisil-alloy [J]. Transactions of Nonferrous Metals Society of China, 2021, 31: 764−778.

[5] MA Li-shi, DUAN Yong-hua, LI Ping. Microstructure, growth kinetics and some mechanical properties of boride layers produced on pure titanium by molten-salt boriding [J]. Journal of Materials Engineering and Performance, 2017, 26: 4544−4555.

[6] MAKUCH N, DZIARSKI P, KULKA M, PIASECKI A, TULIŃSKI M, MAJCHROWSKI R. Influence of niobium and molybdenum addition on microstructure and wear behavior of laser-borided layers produced on Nimonic 80A-alloy [J]. Transactions of Nonferrous Metals Society of China, 2019, 29: 322−337.

[7] ATAR E, KAYALI E S, CIMENOGLU H. Characteristics and wear performance of borided Ti6Al4V alloy [J]. Surface and Coatings Technology, 2008, 202: 4583−4590.

[8] SI Jia-yong, WU Xiao-lin, XIA Ke-nong, ZHANG Ji. Equal channel angular extrusion of TB2 alloy under different die designs by finite element method [J]. Rare Metal Materials and Engineering, 2014: 43: 1577−1581.

[9] WANG Zhi-ming , CHEN Zhi-yong, ZHAN Cong-kun, KUANG Lian-jun, SHAO Jian-bo, WANG Ren-ke, LIU Chu-ming. Quasi-static and dynamic forced shear deformation behaviors of Ti−5Mo−5V−8Cr−3Al alloy [J]. Materials Science and Engineering A, 2017, 691: 51−59.

[10] LI Ping, LIU Dan, BAO Wei-zong, MA Li-shi, DUAN Yong-hua. Surface characterization and diffusion model of pack borided TB2 titanium alloy [J]. Ceramics International, 2018, 44: 18429−18437.

[11] LIU Dan, DUAN Yong-hua, BAO Wei-zong, PENG Ming-jun. Characterization and growth kinetics of boride layers on Ti−5Mo−5V−8Cr−3Al alloy by pack boriding with CeO_2 [J]. Materials Characterization, 2020, 164: 110362.

[12] HUANG Y G, CHEN J R, ZHANG X H, WANG H Q, FANG Z, LI Q Y. Effects of La_2O_3 on electrolytic boronising of titanium [J]. Surface Engineering, 2015, 31: 570−574.

[13] ZHU Yan-song, YIN Yu-xuan, WU Jun, LIU Yun-fei, LU Wen-zhuang, ZUO Dun-wen, XIAO He-ping, CAO Da-wei, KO Tae-jo. Effect of RE on accelerating the kinetics of boride layer growth on titanium alloy [J]. Journal of Alloys and Compounds, 2020, 844: 156091.

[14] DUAN Yong-hua, LIU Dan. HE Bang-lin, MA Li-shi, HU Yan-yun, LI Xiao-qiang. Experimental investigations of TB2 alloy by pack boriding with rare-earth oxides [J]. Philosophical Magazine Letters, 2019, 98: 521−526.

[15] YANG Lei, WANG Bao-yu, LIU Gang, ZHAO Hui-jun, ZHOU Jing. Hot tensile behavior and self-consistent constitutive modeling of TA15 titanium alloy sheets [J]. Journal of Materials Engineering and Performance, 2015, 24: 4647−4655.

[16] LV Xiao-jun, HU Ling-yun, SHUANG Ya-jing, LIU Jian-hua, LAI Yan-qing, JIANG Liang-xing, LI Jie. The growth behavior of titanium boride layers in α and β phase fields of titanium [J]. Metallurgical and Materials Transactions A, 2016, 47: 3573−3579.

[17] LI D X, PING D H, LU Y X, YE H Q. Characterization of the microstructure in TiB-whisker reinforced Ti alloy matrix composite [J]. Materials Letters, 1993, 16: 322−326.

[18] KAESTNER P, OLFE J, RIE K T. Plasma-assisted boriding of pure titanium and TiAl6V4 [J]. Surface and Coatings Technology, 2001, 142−144: 248−252.

[19] LU Y H, ZHOU Z F, SIT P, SHEN Y G, LI K Y, CHEN H.

X-ray photoelectron spectroscopy characterization of reactively sputtered Ti−B−N thin films [J]. Surface and Coatings Technology, 2004, 187: 98−105.

[20] HUANG Feng, LIU W J, SULLIVAN J F, BARNARD J A, WEAVER M L. Room-temperature oxidation of ultrathin TiB_2 films [J]. Journal of Materials Research, 2002, 17: 805−813.

[21] BELYANSKY M, TRENARY M. Reflection adsorption infrared spectroscopy of the oxidation of thin films of boron and hafnium diboride grown on Hf(0001) [J]. Journal of Vacuum Science and Technology A, 1997, 15: 3065−3068.

[22] YADAV A A, LOKHANDE A C, KIM J H, LOKHADE C D. Supercapacitive activities of porous La_2O_3 symmetric flexible solid-state device by hydrothermal method [J]. International Journal of Hydrogen Energy, 2016, 41: 18311−18319.

[23] ZHANG Mao-feng, YUAN Liang, WANG Xiao-qing, FAN Hai, WANG Xu-yang, WU Xue-ying, WANG Hai-zhen, QIAN Yi-tai. A low-temperature route for the synthesis of nanocrystalline LaB_6 [J]. Journal of Solid State Chemistry, 2008, 181: 294−297.

[24] AKGÜN B, SEVINÇ N, ÇAMURLU H E, TOPKAYA Y. Volume combustion and mechanochemical syntheses of LaB_6 [J]. International Journal of Materials and Product Technology, 2017, 55: 331−339.

[25] SARMA B, CHANDRAN K S R. Accelerated kinetics of surface hardening by diffusion near phase transition temperature: Mechanism of growth of boride layers on titanium [J]. Acta Materialia, 2011, 59: 4216−4228.

[26] JAMES C W, EDGAR A S Jr. Progress in structural materials for aerospace systems [J]. Acta Materialia, 2003, 51: 5775−5799.

[27] SUN Shi-bo, WANG Hai-bin, LIU Xue-mei, LIU Chao, LU Hao, NIE Zuo-ren, SONG Xiao-yan. Outstanding anti-oxidation performance of boride coating under high-temperature friction [J]. Corrosion Science, 2021, 179: 109133.

[28] EBRAHIMI A, ESFAHANI H, IMANTALAB O, FATTAH-ALHOSSEINI A. Biological, antibacterial activities and electrochemical behavior of borided commercially pure titanium in BSA-containing PBS [J]. Transactions of Nonferrous Metals Society of China, 2020, 30: 944−957.

[29] LV Jin-long, LIANG Tong-xiang, WANG Chen. Surface enriched molybdenum enhancing the corrosion resistance of 316L stainless steel [J]. Materials Letters, 2016, 171: 38−41.

[30] CHENG Y F, WILMOTT M, LUO J L. Analysis of the role of electrode capacitance on the initiation of pits for A516 carbon steel by electrochemical noise measurements [J]. Corrosion Science, 1999, 41: 1245−0256.

[31] HLADKY K, DAWSON J L. The measurement of corrosion using electrochemical noise [J]. Corrosion Science, 1982, 22: 231−237.

[32] MANSFELD F, SUN Z. Technical note: Localization index obtained from electrochemical noise analysis [J]. Corrosion, 1999, 55: 915−918.

[33] LEE C C, MANSFELD F. Analysis of electrochemical noise data for a passive system in the frequency domain [J]. Corrosion Science, 1998, 40: 959−962.

[34] COTTIS R A. Interpretation of electrochemical noise data [J]. Corrosion, 2001, 57: 265−285.

[35] FUKUDA T, MIZUNO T. The evaluation of pitting corrosion from the spectrum slope of noise fluctuation on iron and 304 stainless steel electrodes [J]. Corrosion Science, 1996, 38: 1085−1091.

[36] FLIS J, DAWSON J L, GILL J, WOOD G C. Impedance and electrochemical noise measurements on iron and iron-carbon alloys in hot caustic soda [J]. Corrosion Science, 1991, 32: 877−892.

La_2O_3 包埋渗硼 TB2 钛合金的腐蚀与磨损性能

曲德艺，刘 丹，王昕宇，段永华，彭明军

昆明理工大学 材料科学与工程学院，昆明 650093

摘 要：为了改善 TB2 合金的表面性能，采用 4%La_2O_3(质量分数)包埋渗硼法对 TB2 合金进行 1100 ℃，20 h 渗硼处理，研究 TB2 钛合金的渗硼层组成与厚度以及腐蚀与磨损性能。结果表明，La_2O_3 在渗硼过程中促进硼化物层的生长，提高其连续性和致密性，TiB 晶须长度从 16.80 增至 21.84 μm。这是因为 La_2O_3 能与 B 反应生成 La−B 活性基团，进一步促进硼化物层的生长。La_2O_3 包埋渗硼能提高 TB2 合金的耐磨性和耐蚀性。未渗硼和渗硼 TB2 合金的磨损机制分别为粘着磨损和磨粒磨损，腐蚀机制从局部腐蚀(未渗硼 TB2 合金)转变为均匀腐蚀(渗硼 TB2 合金)。

关键词：TB2 合金；包埋渗硼；磨损性能；腐蚀性能

(Edited by Bing YANG)